Received: 13 September 2022 | Revised: 16 May 2023 | Accepted: 5 July 2023

DOI: 10.1002/eqe.3976

WILEY

RESEARCH ARTICLE

Modeling uncertainty of specimens employing spines and force-limiting connections tested at E-defense shake table

Bryam Astudillo[1] | **David Rivera**[2] | **Jessica Duke**[3] | **Barbara Simpson**[1] | **Larry A. Fahnestock**[4] | **Richard Sause**[3] | **James Ricles**[3] | **Masahiro Kurata**[5] | **Taichiro Okazaki**[6] | **Yohsuke Kawamata**[7] | **Zhuoqi Tao**[4] | **Yi Qie**[6]

[1]Department of Civil and Environmental Engineering, Stanford University, Stanford, California, USA

[2]School of Civil and Construction Engineering, Oregon State University, Corvallis, Oregon, USA

[3]Department of Civil and Environmental Engineering, Lehigh University, Bethlehem, Pennsylvania, USA

[4]Department of Civil and Environmental Engineering, University of Illinois Urbana-Champaign, Urbana, Illinois, USA

[5]Disaster Prevention Research Institute, Kyoto University, Kyoto, Japan

[6]Division of Architectural and Structural Design, Hokkaido University, Sapporo, Japan

[7]Hyogo Earthquake Engineering Research Center, National Research Institute for Earth Science and Disaster Resilience, Miki-shi, Japan

Correspondence
Bryam Astudillo, Department of Civil and Environmental Engineering, Stanford University, Stanford, California, USA.
Email: bastudil@stanford.edu

Funding information
American Institute of Steel Construction; National Science Foundation, Grant/Award Numbers: 1928906, 1926326, 1926365; Disaster Prevention Research Institute, Kyoto University; Japan Society for the Promotion of Science, Grant/Award Number: 20H00269

Abstract

In light of the significant damage observed after earthquakes in Japan and New Zealand, enhanced performing seismic force-resisting systems and energy dissipation devices are increasingly being utilized in buildings. Numerical models are needed to estimate the seismic response of these systems for seismic design or assessment. While there have been studies on modeling uncertainty, selecting the model features most important to response can remain ambiguous, especially if the structure employs less well-established lateral force-resisting systems and components. Herein, a global sensitivity analysis was used to address modeling uncertainty in specimens with elastic spines and force-limiting connections (FLCs) physically tested at full-scale at the E-Defense shake table in Japan. Modeling uncertainty was addressed for both model class and model parameter uncertainty by varying primary models to develop several secondary models according to pre-established uncertainty groups. Numerical estimates of peak story drift ratio and floor acceleration were compared to the results from the experimental testing program using confidence intervals and root-mean-square error. Metrics such as the coefficient of variation, variance, linear Pearson correlation coefficient, and Sobol index were used to gain intuition about each model feature's contribution to the dispersion in estimates of the engineering demands. Peak floor acceleration was found to be more sensitive to modeling uncertainty compared to story drift ratio. Assumptions for the spine-to-frame connection significantly impacted estimates of peak floor accelerations, which could influence future design methods for spines and FLC in enhanced lateral-force resisting systems.

KEYWORDS

floor accelerations, force-limiting connections, global sensitivity analysis, higher modes, modeling uncertainty propagation, steel spines

1 | INTRODUCTION

Numerical models are needed to estimate structural response, develop rational and practical engineering design solutions, and reduce reliance on experimental testing. However, numerical models are subject to modeling uncertainty.[1,2] For example, blind prediction contests have shown that modeling uncertainty can considerably affect estimates of dynamic response,[3–5] influencing simulated behavior modes and demand estimates used for design. Although the behavior of many traditional seismic force-resisting systems is well-documented and characterized,[6–9] numerical models of lateral force-resisting systems are still subject to appreciable modeling uncertainty.[10–13]

Modeling uncertainty can be even greater when estimating the response of less well-established structural systems and components. If not codified, new lateral-force resisting systems are subject to designs using alternative methods,[14] which are often based on performance-based design philosophies. In performance-based design, the trustworthiness of the structural design relies on the fidelity of the numerical model.[15–20] Many performance assessment methodologies, such as FEMA P-695[21] and FEMA P-58,[22] consider modeling uncertainty by categorizing the fidelity of the numerical model and adjusting the fragility function accordingly. However, the seismic demands estimated for the structural and nonstructural components can be affected by the use of a unique numerical model that does not directly account for modeling uncertainty.[4,23]

Often, the model features most important to estimating response are ambiguous, making it difficult to represent the full range of potential structural demands using a unique numerical model. Story drifts are often used in collapse assessment or to characterize structural and drift-sensitive nonstructural damage.[12,16,18] On the other hand, floor accelerations characterize the forces in structural systems and the demands on acceleration-sensitive nonstructural components.[15] However, changing the properties of the numerical model can change the estimates of the drifts and accelerations; for example, as observed for reinforced concrete shear-wall buildings, particularly at low ground motion intensity levels.[10] Assumptions for viscous damping have been found to affect acceleration response.[10] Increases in story drifts due to modeling uncertainty can also result in an increased mean annual frequency of collapse, for example, as observed for reinforced concrete buildings.[18]

Because the relative importance of a model feature to the estimated response depends on the structural system, ground motion intensity, and available data, blind predictions prior to an experiment remain especially challenging. Since estimates of drifts and floor accelerations for shake-table tests depend on the adopted model assumptions, post-test numerical models are often adjusted to improve estimates of shake-table response, as in Grange et al.[11] For example, blind predictions of a near single-degree-of-freedom concrete column tested at the University of California, San Diego shake table were biased by 5%–35% for drifts and from 25 to 118% for accelerations.[4] Dispersion would be expected to be larger for more complex structural systems, where there are more sources of uncertainty.

The modeling assumptions used in a unique model can result in estimated demands that do not represent the range of possible response of a test specimen. For example, in a blind prediction study of fixed-base and base-isolated five-story steel moment resisting frames (MRF), floor accelerations were overestimated in the high-frequency range by the pretest numerical model, even though the models well represented accelerations in the low-frequency range.[23] For the same experiments, modeling the composite floor action was found to be important in representing the specimen's stiffness.[24] Assumptions for damping in the higher modes influenced estimates of the peak acceleration response.[24] Other studies have found that smooth force–deformation relations produce smaller peak accelerations compared to bilinear force–deformation relations,[25] while material softening little affects estimates of floor accelerations in special MRF.[25]

For less well-characterized structural systems, modeling uncertainty could be even larger than for traditional lateral force-resisting systems, because the structural behavior is less well known. For example, the numerical response of steel rocking braced frames has been found to depend on modeling of the energy dissipators, frame components, and gravity loading, depending on the performance level.[20] Enhanced performing structural systems and energy dissipating devices will continue to be developed,[26–28] motivated by efforts to enhance post-earthquake re-occupancy and recovery time-to-functionality.[29–31] Moreover, reliance on numerical models will increase with the industry's adoption of performance-based design and nonlinear analysis of structures,[32,33] which is often needed for the design of new or novel structural systems. The sources of modeling uncertainty for these new types of structural systems still need to be identified and characterized to better understand their behavior and performance and to, ultimately, facilitate their adoption in industry.

Efforts to address modeling uncertainty need to be extended to assess the response of new structural systems and components. Although it is important to explicitly address modeling uncertainty to estimate demands on drift-sensitive and acceleration-sensitive components, incorporation of modeling uncertainty results in substantial amounts of data, which

then need to be analyzed to determine the model features and decisions most relevant to the seismic response. Understanding the results of such analyses require extensive post-processing and modeling expertise. Thus, metrics need to be selected to ease the interpretation of the resulting data from the uncertainty analysis and to identify the most salient model features.

Herein, the effects of modeling uncertainty are studied for a relatively new steel system consisting of a traditional MRF, elastic steel spines, and force-limiting connections (FLC). The combined Frame–Spine–FLC system was tested at the E-Defense shake table facility in Japan.[34–37] In these systems, vertical elastic spines impose a more uniform drift distribution over the building height to mitigate story mechanisms.[38–41] Additionally, FLC with yielding elements, placed between the spine and MRF, control the magnitude of the forces transferred between the spine and MRF,[42–45] thereby limiting higher-mode accelerations and force demands that tend to develop in systems with elastic spines.[46] Due to the presence of the spine and FLC, designs of these types of enhanced lateral-force resisting systems can be highly affected by estimates of story drifts and floor accelerations, which are also affected by modeling uncertainty.[20] In including modeling uncertainty, this study identified the model features of greatest influence to the response of the test specimens and illustrates the variability in drifts and acceleration demands for different sources of modeling uncertainty, particularly for the spine-to-frame connection.

Global sensitivity analyses were used to characterize the effects of modeling uncertainty in the shake-table testing program. Sources of modeling uncertainty were identified for pretest numerical models accompanying the full-scale testing program.[37,47] Two ground motions with different spectral characteristics used in the experimental testing program were used to assess the sensitivity of select Engineering Demand Parameters (EDPs) to variations of the numerical model. Sources of modeling uncertainty were categorized into five uncertainty groups, including uncertainty in modeling the: [i] beam, [ii] panel zone, [iii] damping, [iv] mass, and [v] spine-to-frame connection (either bolted connection or FLC depending on the test specimen). The EDP estimates (i.e., peak story drifts θ and peak floor accelerations PFA), including modeling uncertainty, were analyzed and compared to the experimental results[36,37] using confidence intervals and root-mean-square error e_{EDP}. Results from the suite of analyses were interpreted using the coefficient of variation COV, variance σ^2, linear Pearson correlation coefficient ρ, and the Sobol Index,[48] which combined are useful in interpreting numerical results incorporating modeling uncertainty. In particular, the total Sobol index S_T measures the influence of one model parameter to the EDP variance, while incorporating its interactions with variations in other model parameters.

Beyond the experimental testing program, the modeling uncertainty approach used herein could be adapted to inform post-test modeling calibrations, other experimental testing programs, and future design methods, such as placement and strength of the FLC based on floor acceleration response, among other design considerations. Ultimately, directly accounting for modeling uncertainty can provide more information about expected structural behavior and, therefore, aid decision-makers in considering a greater set of possible design solutions and variations in structural response.

2 | TREATMENT OF MODELING UNCERTAINTY

Modeling uncertainty arises from limited knowledge of choosing between modeling alternatives and formulations, or model classes (i.e., epistemic uncertainty) and from randomness in material mechanical properties, geometric or dimensional properties, loads, and so forth (i.e., aleatory variability). Varying the deterministic model class[13] and continuous model parameters[16] can lead to smaller or larger departures in the estimated response, depending on the sensitivity of the response to that model feature. Herein, the sensitivity of the output EDP to each model input X_i was assessed using global sensitivity analysis via Sobol indices[48] and correlation coefficients. The resulting EDPs and their dispersion due to the presence of modeling uncertainty were used to systematically estimate the anticipated specimen response prior to the shake table testing program, to interpret the data and determine which model features most influence each EDP, and to gain an intuition of how the model classes and parameters affect the peak EDPs (e.g., those corresponding to the spine-to-frame connection).

2.1 | Random variables for deterministic model classes and continuous model parameters

The dynamic response of the shake-table test specimens was explored using sets of numerical models, referred to as primary and secondary models. The primary models were developed with best-estimate, or nominal, model classes and model

parameters chosen prior to the experiment. The secondary models were developed from the primary models by varying the model classes and model parameters according to random variables in five uncertainty groups representing the following components: [i] beam, [ii] panel zone, [iii] damping, [iv] mass, and [v] spine-to-frame connection. To address epistemic uncertainty, the model class was deterministically varied from a set of preselected options according to a categorical random variable; for example, the spine-to-frame connection was modeled using four different model classes (each class having a similar probability of occurrence), to generate secondary models. To address aleatory variability, model parameters were considered continuous (i.e., with values lying in an interval of real numbers) and represented by continuous random variables following pre-established probability density functions (PDF).

The Frame, Frame–Spine, and Frame–Spine–FLC models have 12, 13, and 16 random variables, respectively, which are detailed in the next section. Although others have found that correlation between random variables can lead to further dispersion in the estimated response[49–51] and have proposed methods to inform correlation values for the model inputs,[51,52] uncorrelated input random variables were used here to gain intuition in the separate effect of each variable and to assess the contribution of each independent random variable to the output variance (i.e., without results being driven by the changes in other variables).

The sampling for the global sensitivity analysis was generated in quoFEM[53,54] using the Dakota uncertainty quantification engine[55] and Latin hypercube sampling.[56] On the backend, the sampling scheme, in agreement with the formulation of the Sobol index[48,57,58] described next, involved generating two sets of independent samples for each of the random variables associated with a numerical model (e.g., two matrices $\mathbf{A}$ and $\mathbf{B}$ of size $n \times d$, where n is the number of samples for one random variable, d is the number of random variables, and collectively the values of each row k are the inputs needed in one model for one simulation); then, additional sets of samples were obtained by systematically combining the columns of the two original sets to form $\mathbf{A}_{\mathbf{B}}^{(i)}$ (random variables with samples from $\mathbf{A}$, except for X_i which has the samples from $\mathbf{B}$). Combined, the samples from $\mathbf{A}$, $\mathbf{B}$, and $\mathbf{A}_{\mathbf{B}}^{(i)}$ lead to a total of $n \times (d + 2)$ simulations per specimen.

2.2 | Data processing

The relative dispersion of the estimated EDPs was represented by the coefficient of variation, $COV_Y = \sigma_Y / \mu_Y$, where σ_Y is the standard deviation and μ_Y is the mean of the quantity of interest Y; herein, the EDPs correspond to peak story drift ratio θ_j and peak floor acceleration PFA_j at story/floor j. Some model classes and parameters had a more pronounced influence on the dispersion of the EDP (measured by the variance σ^2_{EDP}); the influence was addressed using a global sensitivity study with a variance-based approach, which allows a full exploration of the input space as opposed to local sensitivity studies. To characterize the effects of modeling uncertainty, the variances of the maximum responses, σ^2_{EDP}, were decomposed via Sobol indices[48] to assess the contributions of each random variable to the overall variance. The total Sobol indices S_{Ti} were used to account for the contribution to the variance attributed to each variable X_i and its interactions with the rest of the random variables $\mathbf{X}_{\sim i}$ (Equation 1[48,57]). The estimator for the total sensitivity index is indicated in Equation (2).[58] A larger S_T indicates a greater sensitivity of Y to a particular random variable X_i, and, therefore, the uncertainty contained in X_i becomes a larger contribution to the uncertainty of Y (i.e., contribution of modeling uncertainty to the dispersion of the EDP estimates θ and PFA).

$$S_{Ti} = \frac{E_{\mathbf{X}_{\sim i}}(V_{X_i}(Y|\mathbf{X}_{\sim i}))}{V(Y)} = 1 - \frac{V_{\mathbf{X}_{\sim i}}(E_{X_i}(Y|\mathbf{X}_{\sim i}))}{V(Y)} \tag{1}$$

$$\hat{S_{Ti}} = \frac{\frac{1}{2n}\sum_{k=1}^{n}(f(\mathbf{A})_k - f(\mathbf{A}_{\mathbf{B}}^{(i)})_k)^2}{\left(\frac{1}{2n}\sum_{k=1}^{2n}(f(\mathbf{C})_k)^2\right) - \left(\frac{1}{2n}\sum_{k=1}^{2n} f(\mathbf{C})_k\right)^2} \tag{2}$$

where V and E denote the variance and expectation operator, respectively; $f(.)_k$ corresponds to one value of the output Y resulting from one simulation with the sample inputs from the kth row in the matrix $(.)$; and, $\mathbf{C}$ concatenates the samples from $\mathbf{A}$ and $\mathbf{B}$.

In addition, the relationship between the input random variable X_i and the output EDP_j was represented by the linear Pearson correlation coefficient $\rho(X_i, EDP_j)$, ranging from ± 1 to gain insight on the effects of a particular model parameter; -1 indicates a perfect negative correlation, 0 indicates no correlation, and $+1$ indicates a perfect positive correlation.

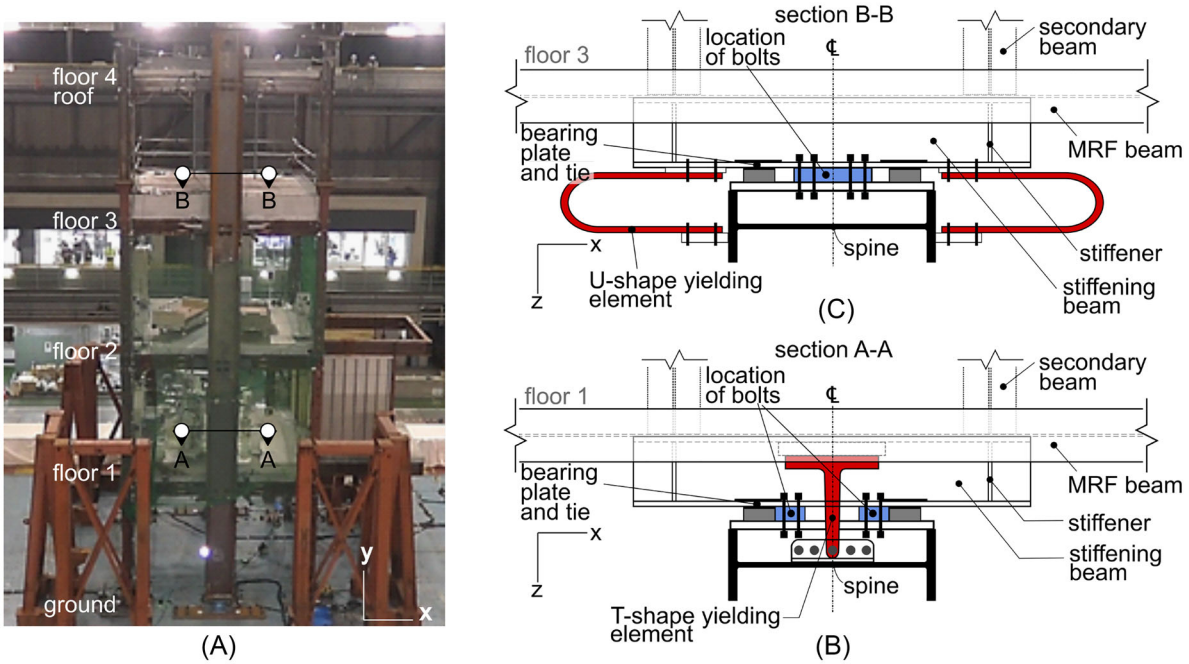

FIGURE 1 Schematic of: (A) full-scale specimen at E-Defense, (B) Floor 1 spine-to-frame connection, and (C) Floor 3 spine-to-frame connection.

These types of metrics (e.g., S_{Ti} and $\rho(X_i, EDP_j)$) can then be used to select the model features that most affect the variability of the numerical estimates and to gain intuition on their effects, for example, to enhance numerical simulations or design methods.

3 | EXPERIMENT TESTING PROGRAM

The EDP estimates, including modeling uncertainty, were studied for a shake-table testing program at E-Defense. As a relatively new structural system, the Frame–Spine–FLC system used less well-established structural components and energy dissipators compared to traditional lateral-force-resisting systems. Thus, modeling uncertainty was paramount to estimating the range of possible response and to gaining intuition on the effects of the model components.

3.1 | Test specimens

The testing program was comprised of three test specimens: (a) Frame, (b) Frame–Spine, and (c) Frame–Spine–FLC. The full-scale specimens consisted of a four-story steel building containing acceleration-sensitive medical equipment representative of a hospital facility; see Figure 1A. The shaking was applied in the direction of the *x*-axis; more details of the testing program can be found in Refs. [34–37, 47].

The Frame specimen consisted of an MRF-only specimen, which was studied numerically but not experimentally. The MRF with pinned base was susceptible to forming a severe story mechanism in the first story.[37,59] As the specimen utilized an existing three-story specimen designed for another testing program, the first three stories of the Frame specimen included details consistent with Japanese practice with hollow square sections for the columns and wide-flange beams. The fourth story, added later for this testing program, included details consistent with U.S. practice for MRF panel zone and column sections. Yielding was expected to occur in the panel zones rather than the beams during the shake-table testing. To add mass to achieve reasonable dynamic properties, a thick concrete slab of 610 mm was located on the third floor, and steel plates were fastened to the roof. Shear studs were placed every 300 mm to connect the concrete slab to the steel beams. A clearance of 25 mm was expected between the slab and column faces.

The Frame–Spine specimen consisted of elastic spines attached to the pinned-base MRF. The spines were attached to the exterior of the MRF specimen via stiffening beams and slip-critical bolted connections; see the location of the bolts

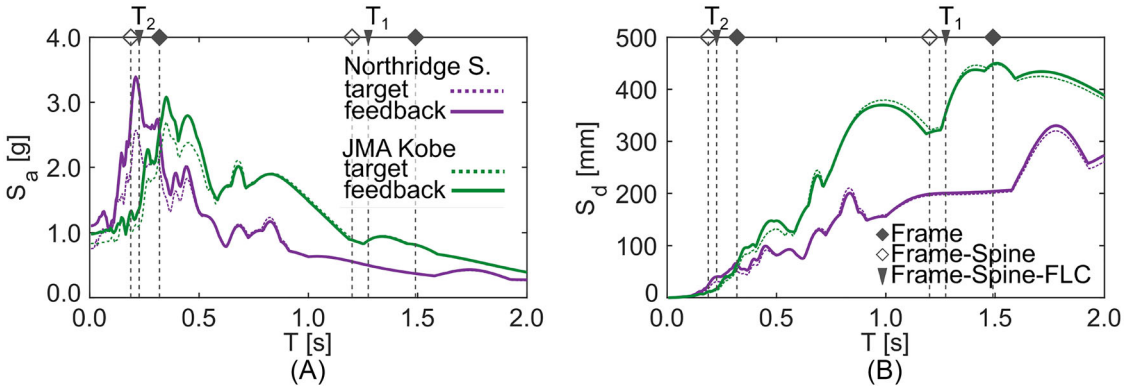

FIGURE 2 Response spectra: (A) pseudo-acceleration S_a and (B) spectral displacement S_d of the Northridge and JMA Kobe record records.

highlighted in Figure 1B,C. At each connection to the stiffening beam in the loading plane, the spine was restrained from translation in the *x*- and *y*-axes, and partially restrained to rotate about the *z*-axis.

The Frame–Spine–FLC specimen consisted of elastic spines attached to the pinned-base MRF using the FLC. The spines were attached to the exterior of the MRF specimen via stiffening beams and FLC. The Floor 1 FLC consisted of the tension ties, bearing plates, and two T-shape yielding elements in Figure 1B; the Floor 2 FLC consisted of tension ties and bearing plates; and the Floor 3 FLC consisted of the tension ties, bearing plates, and U-shape yielding elements in Figure 1C. The spine-to-frame connection at Floor 4 consisted of the same slip-critical bolted connection utilized in the Frame–Spine specimen. For testing purposes, the bolted connection and FLC were assembled using the same MRF specimen, as shown in Figure 1, and the bolted connections were unbolted to release the FLC for the Frame–Spine–FLC specimen.

3.2 | Ground motion records

Two ground motion records were used for the experimental testing program, isolating the effects of record-to-record variability from the modeling uncertainty. The ground motions had different spectral characteristics, as highlighted in Figure 2; the first two modal periods of the models are indicated for reference. The unscaled Sepulveda Valley Hospital record from the 1994 Northridge earthquake had large pseudo-accelerations near the second-mode period of the specimens. The unscaled JMA-NS Kobe record from the 1995 Kobe earthquake had large spectral displacements near the first-mode period of the specimens. For subsequent comparisons, the two ground motion records were replaced by the measured acceleration of the E-Defense shake table. The selection of the ground motions and the effects of record-to-record variability are described in Refs. [36, 37].

4 | NUMERICAL MODELS

Two-dimensional numerical models of the test specimens were developed in OpenSees[60]; see Figure 3A. Three primary models were developed to represent the initial estimate of the Frame, Frame–Spine, and Frame–Spine–FLC specimen properties and were used to benchmark the specimens' behavior prior to testing.[37] Modeling uncertainty was addressed via a global sensitivity study using the methods outlined in Section 2 and a set of secondary models derived from varying the primary models according to predetermined uncertainty groups.

4.1 | Primary models

The primary models were developed to simulate the test specimens, estimate nominal natural periods, and characterize general behavior under a suite of ground motions and amplitude scaling factors.[37] As the "best guess" prior to experimental testing, these models were used as a starting point to incorporate modeling uncertainty.

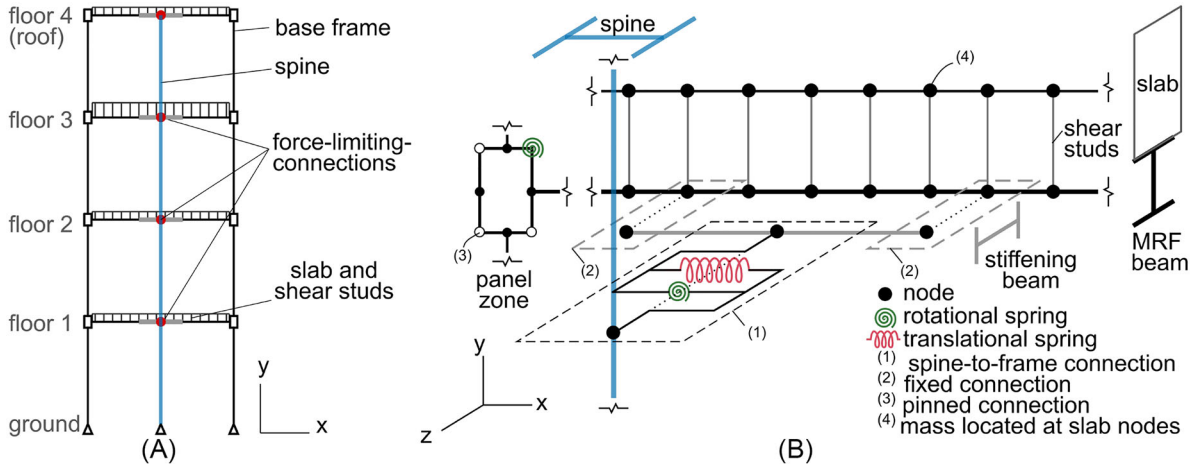

FIGURE 3 Schematic of: (A) overall numerical model and (B) details of panel zone, composite beam, and spine-to-frame connection models.[37]

TABLE 1 Sections and components used in Frame, Frame–Spine, and Frame–Spine–FLC specimens.

Story/floor	Story heights [mm]	Columns	Beams	$t_s j$ [mm]	Stiffening beam	Spine	Spine-to-frame connection	
							Frame–Spine	Frame–Spine–FLC
4th	3500	W10×100[a]	W16×40[a]	150	W10×68[a]	W30×148[a]	Bolted[d]	Bolted[d]
3rd	3500	□ 250 × 250×9[b]	H400×200 × 8×13[c]	610	W10×68[a]	W30×148[a]	Bolted[d]	Floor 3 FLC[e]
2nd	3500	□ 250 × 250×9[b]	H400×200 × 8×13[c]	150	W10×68[a]	W30×148[a]	Bolted[d]	Floor 2 FLC[f]
1st	3281	□ 250 × 250×9[b]	H400×200 × 8×13[c]	150	W10×68[a]	W30×148[a]	Bolted[d]	Floor 1 FLC[g]

Nominal yield stress, F_y:
[a]380.2 N/mm^2 (A992);
[b]364.9 N/mm^2 (BCR295),
[c]344.7 N/mm^2 (SN490B).
Spine-to-frame connection:
[d]slip-critical bolted connection;
[e]U-shape yielding element, tension tie, bearing plates;
[f]tension tie, bearing plates;
[g]T-shape yielding element, tension tie, bearing plates.
$t_s j$ = slab thickness. Bay width = 5000 mm.

To account for the small damping associated with the bare frame test specimen, the primary model for all specimens used Rayleigh damping with a target damping ratio of 0.5% at an elongated first-mode period, $1.5T_1$, and third-mode period, T_3. The beams and columns were modeled using force-based beam–column elements with five integration points, a Gauss–Lobatto integration scheme, and multiple fibers across the section (5 across the W/H web depth and flange thickness and HSS wall thickness and depth) based on a sensitivity study.[36] The integration points at the ends of the beams and columns were shifted away from the faces of the beam–column connections using an additional node at a distance of half the element depth. The beams and columns were modeled with Corotational and P-Delta geometric transformations, respectively. As the spine was expected to remain elastic, the spine was modeled with elastic beam–column elements; post-processing of the data using the primary models confirmed that the spine remained in the elastic range. The analyses used Newmark's constant average acceleration integrator starting with the Newton–Krylov algorithm. The time step was adaptive, with a maximum time step of half the ground motion sampling time.

Figure 3B illustrates an exploded view of the components of the numerical model. These primary models accounted for composite-beam action, panel zone yielding, and influence of the stiffening beams, as indicated in the subsequent description of the model components and uncertainty groups. Material properties, model classes, and model parameters were defined a priori based on engineering judgment, data from coupon testing, testing of the FLC yielding elements, and supplemental experiments of beam–column connections,[34,35,47,61,62] as summarized in Tables 1 and 2. Uniaxial materials

TABLE 2 Nominal values used in Frame, Frame–Spine, and Frame–Spine–FLC models.

Story/ floor	Weights, $m_j g$ [kN]	$b_e j$ [mm]	Panel zones			Frame–Spine	Frame–Spine–FLC	
			γ_y, [rad×10⁻2]	$V_y d_b$, [kN-m]	$V_p d_b$, [kN-m]	Bolted	K [kN/mm]	P [kN]
4th	548	410	0.313	433.4	572.4	[a]	-	-
3rd	534	410	0.321	338.6	410.8	[a]	3.4[b]	54[b]
2nd	175	410	0.321	338.6	410.8	[a]	-	-
1st	264	410	0.321	338.6	410.8	[a]	22.9[b]	261[b]

m_j = mass of floor j; b_e= slab effective width, γ_y= panel zone shear deformation at yield, V_y = panel zone shear strength, V_p = panel zone ultimate strength, d_b = beam depth.

[a]See bolted connection assumptions in Figure 4.

[b]Value for two yielding elements.

K = initial stiffness of the yielding elements, P = strength of the yielding elements.

TABLE 3 Random variables used in the generation of the secondary models clustered by uncertainty group.

Modeling uncertainty group	#[a]	Random variables[b]	Description
i. Beam composite action	4	$X_{be}^{j} \sim U(400, 650)$ mm	Continuous model parameters for $b_e j$
ii. Panel zone	3	$X_{pz,K_e} \sim U(0.90, 1.10)$	Continuous model parameter for the panel zone K_e, V_y, and V_p
		$X_{pz,V_y} \sim U(0.90, 1.10)$	
		$X_{pz,V_p} \sim U(0.80, 1.20)$	
iii. Damping	1	$X_{\zeta} \sim U(0.1, 2.5)\,\%$	Continuous model parameter for ζ
iv. Mass	4	$X_{m}^{j} \sim U(0.95, 1.05)$	Continuous model parameters for m_j
v. Spine-to-frame connection			
Bolted connection	1	$X_{bc} \sim \{C1, C2, C3, C4\}$[c]	Deterministic bolted connection model classes
FLC	4	$X_{K}^{1} \sim U(0.50, 0.80)$	Continuous model parameters for the Floor 1 FLC and Floor 3 FLC stiffness and strength, based on K_T, P_T, K_U, and P_U
		$X_{P}^{1} \sim U(0.80, 1.20)$	
		$X_{K}^{3} \sim U(0.80, 1.20)$	
		$X_{P}^{3} \sim U(0.80, 1.20)$	

[a]Number of random variables related to the uncertainty group; the Frame, Frame–Spine, and Frame–Spine–FLC secondary models have 12, 13, and 16 random variables, respectively. One hundred samples were used per random variable, leading to 1400, 1500, and 1800 secondary models for the Frame, Frame–Spine, and Frame–Spine–FLC specimens.

[b]$X \sim U(a, b)$ indicates that the random variable X follows a uniform distribution with values between a and b.

[c]The deterministic model classes are indicated in Figure 4.

included: (a) the beams' and columns' structural steel and FLC properties modeled with a Menegotto–Pinto relationship; (b) the slab, which had significant steel reinforcement, was idealized with a bilinear relationship to represent a reinforced concrete slab assuming a strength of 21 MPa (3000 psi); and (c) the panel zone force–deformation behavior used a trilinear relationship, described in more detail subsequently.

4.2 | Secondary models

The secondary models were derived from the primary models within each uncertainty group, defined by the: [i] beam, [ii] panel zone, [iii] damping, [iv] mass, and [v] spine-to-frame connection models (either bolted connection or FLC depending on the test specimen). The Frame, Frame–Spine, and Frame–Spine–FLC models have 12, 13, and 16 random variables (with 100 samples per random variable), respectively. The total number of secondary models to conduct the global sensitivity analysis of the Frame, Frame–Spine, and Frame–Spine–FLC models were 1400, 1500, and 1800 secondary models, respectively. The uncertainty groups and random variables employed in the secondary models are highlighted in Table 3 and discussed in greater detail in the next section. To summarize the uncertainty groups and random variables:

(i) In the beam uncertainty group, the continuous model parameters $X_{b_e}^{j}$ defined the effective width b_e of the concrete slab at floor j.

(ii) In the panel zone uncertainty group, the continuous model parameters $X_{pz,K_e}, X_{pz,V_y}, X_{pz,V_p}$ defined the elastic stiffness, yielding, and plastic shear strength of the panel zones based on their nominal values K_e, V_y, and V_p, respectively.
(iii) In the damping uncertainty group, a continuous model parameter X_ζ defined the target damping ratio ζ.
(iv) In the mass uncertainty group, continuous model parameters X_m^j defined the mass at floor j based on m_j.
(v) In the spine-to-frame connection uncertainty group, models for the Frame–Spine and Frame–Spine–FLC specimens were defined separately. For the Frame–Spine specimen, four deterministic model classes were defined by X_{bc} to define the modeling representation of the bolt patterns in Figure 1B,C. For the Frame–Spine–FLC specimen, continuous model parameters, X_K^1 and X_P^1, defined the stiffness and strength, respectively, of the Floor 1 FLC based on the stiffness and strength of the T-shape yielding element (K_T and P_T). Similarly, continuous model parameters, X_K^3 and X_P^3, defined the stiffness and strength of the Floor 3 FLC based on the stiffness and strength of the U-shape yielding element (K_U and P_U).

5 | MODELING UNCERTAINTY GROUPS

Each of the five uncertainty groups addressed the sources of modeling uncertainty associated with a specific component of the numerical model; more details can be found in Refs. [36, 37].

5.1 | Beam composite action model

The effect of the beam composite action in the experiment was uncertain in terms of the effective width of the one-sided slabs adjacent to the lateral-force resisting system, particularly due to the use of an unusual 610-mm-thick concrete slab to add mass (Table 1). Common methods of estimating the slab effective width b_e for composite beams may over-estimate the beam stiffness with one-sided slabs (e.g., beams located on the exterior of the building as in the specimens).[63] Values for b_e were estimated from $b_e = 0.13L - 0.16s = 410$ mm[64] (where L = beam span length, and s = spacing to neighboring beam in the transverse direction) and $b_e = L/8 = 625$ mm.[63] The composite beam model was modeled with separate sections and elements for the steel beam and concrete slab members connected at the shear stud locations every 300 mm, as shown in Figure 3. To investigate the influence of the slab on the model response, the concrete slab was modeled by stochastically varying the effective width of the slab at each floor j according to a random variable $X_{b_e}^j$ defined by a uniform distribution between 400 and 650 mm. The mass was located at the nodes of the slab elements. Shear stud flexibility, slip, and curvature incompatibilities between shear studs were neglected.

5.2 | Panel zone model

Panel zone yielding was expected for the test specimens. The panel zone was modeled with the Krawinkler parallelogram configuration[65] and a trilinear moment–rotation spring; see Figure 3. The trilinear moment–rotation spring was based on a combination of Japanese[66–70] and U.S. literature.[71–74] Larger or smaller estimates of panel zone strength could result in force redistributions to the beam or surrounding column elements after panel zone yielding.

Nominal yield and plastic moment strengths of the rotational spring, M_y and M_p, were based on the panel zone shear strength, V_y and V_p, multiplied by the depth of the beam, d_b; see values in Table 2. The rotation of the rotational spring represents the panel shear distortion, γ. The plastic shear deformation was modeled as $\gamma_p = 4\gamma_y$, and a post-plastic stiffness was adopted as 3% of the initial stiffness.[74] To investigate the influence of the panel zone on the estimated response, uncertainty was addressed by changing the elastic stiffness, yielding, and post-yielding strength to within ±10%, ±10%, and ±20% of the nominal stiffness K_e and strength V_y and V_p, respectively, via uniform random variables ($X_{pz,K_e}, X_{pz,V_y}, X_{pz,V_p}$). More details on the panel zone calculations can be found in Refs. [36, 37].

5.3 | Damping model

Inherent damping of the bare steel specimens during the shake-table testing was expected to be smaller than that of typical buildings; still, the level of inherent damping was considered uncertain. To investigate the influence of the

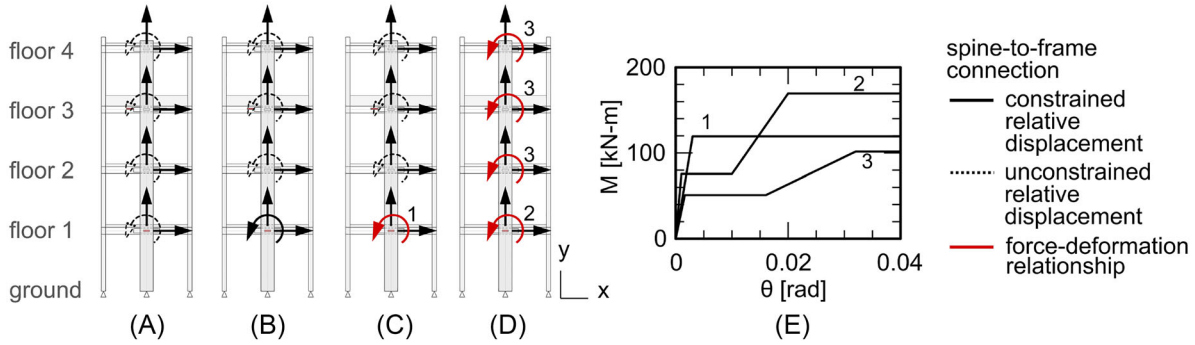

FIGURE 4 Spine-to-frame bolted connection model classes for the Frame–Spine specimen with: (A) constraints in translation only, C1; (B) constraints in translation and rotation, C2; (C) moment–rotation based on the stiffening beam capacity, C3; and (D) moment–rotation relations based on assumed limit states, C4; (E) $M - \theta$ relation of bolted connection.

damping ratio on the model response, ζ was set equal to a random variable X_ζ following a uniform distribution with values ranging from $\zeta = 0.1\%$–2.5%, given the bare steel frame and lack of partition walls or soil–structure interaction.[75–77] All models used Rayleigh damping with the same target periods as the primary model, as differences between damping models, like modal damping, were previously found to have little effect on the selected EDPs for the specimens herein.[36]

5.4 | Mass model

The specimen's dynamic properties depend on estimates of the mass, m. Although the nominal weight of the materials and building dimensions were known prior to testing, the actual mass per floor j was uncertain and treated as a random variable X_m^j. The mass per floor in the structural model was assumed to follow a uniform distribution with a mean equal to the nominal estimate of the primary model in Table 1 and limits of $\pm 5\%$ of the mean. This is a simplification of values proposed by Ellingwood[49] (i.e., normal distribution with COV equal to 10%), given that the specimens were constructed under controlled conditions for laboratory testing.

5.5 | Spine-to-frame bolted connection model

In the Frame–Spine specimen, the spines were attached to the perimeter of the MRF through slip-critical bolted connections. The Frame–Spine specimen had the bolt configuration shown in Figure 1B,C. The figure shows the eccentricity of the bolt pattern from the centroid, which can produce partially restrained moment–rotation behavior. At Floor 1, this eccentricity was larger than that of the other floors to allow for the placement of the T-shape yielding elements that were tested subsequently in the Frame–Spine–FLC test. Although relative translation between the spines and the frame was expected to be small, the moment–rotation behavior of the spine-to-frame connection, in particular the stiffness and strength, was uncertain.

To account for uncertainty in the connection, four models of the spine-to-frame connections were developed for the Frame–Spine specimen; see Figure 4A–D: (a) constrained translation only with free relative rotation and no moment transfer; that is, pinned connections; (b) constrained translation at each floor with constrained rotation at Floor 1 and full moment transfer at Floor 1 (C2); (c) constrained translation at each floor with moment–rotation behavior limited by the stiffening beam capacity at Floor 1 (C3); and (d) constrained translation at each floor with moment–rotation behavior based on slip and yielding behavior estimated for the bolts at each floor level (C4).

For C3, the strength of the connection was assumed to be 80% of the yield moment of the stiffening beam with a yield rotation for partially restrained connections per ASCE 41[78]; see the corresponding moment–rotation ($M - \theta$) relation [1] in Figure 4E. For C4, limit states based on the bolt pattern were assumed based on initiation of bolt slip, followed by restiffening after the bolts have slipped along the slotted holes, and finally yielding of the bolts in shear; see the corresponding $M - \theta$ relations [2] and [3] in Figure 4E.

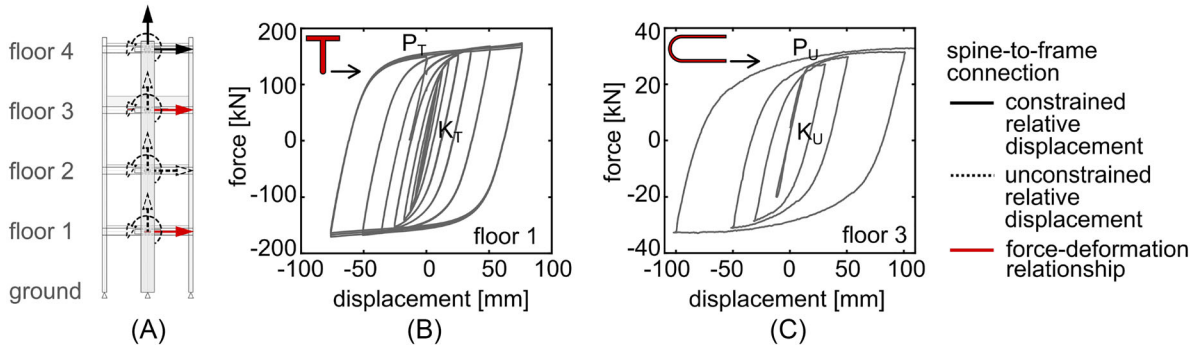

FIGURE 5 FLC models: (A) spine-to-frame connection models for Frame–Spine–FLC specimen, force–deformation relation for (B) T-shape yielding element and (C) U-shape yielding element, adapted from Refs. [35, 37, 62]. FLC, force-limiting connection.

5.6 | Spine-to-frame force-limiting connection (FLC) model

In the Frame–Spine–FLC specimen, the spine was connected to the frame using an FLC with T-shape yielding elements at Floor 1 and an FLC with U-shape yielding elements at Floor 3, see Figure 1C; the connection at Floor 2 did not contain a yielding element, and the connection at the Floor 4 was bolted. Floors 1 and 3 FLC were modeled with zero-length elements connecting the spine to the stiffening beams (see Figures 3B and 5A); no connection was modeled at Floor 2, and the connection at Floor 4 duplicated the pinned condition for the bolted connection of the Frame–Spine specimen. The U-shape yielding elements at Floor 3 can be affected by out-of-plane and other loading conditions arising from the placement eccentricity, which was neglected in the zero-length elements as the Floor 3 FLC was modeled in the lateral translational direction only.

In addition to the T-shape and U-shape yielding elements, the Floor 1 FLC and Floor 3 FLC included a stiffening beam attached to the MRF beam, bearing plates, and ties; see Figure 1B,C. The Floor 3 FLC also included stiffeners at the connections of the U-shape yielding element. Due to a lack of experimental data on the effects of the other FLC components outside of the yielding elements, the force–deformation relationship of the Floor 1 and Floor 3 FLC was uncertain, because the stiffness and strength of the modeled Floor 1 FLC and Floor 3 FLC were estimated from the results of isolated tests of the corresponding yielding elements only.[35,62] The Floor 1 FLC was assumed to have 65% of the stiffness and 100% of the strength of the T-shape yielding elements (i.e., $0.65K_T$ and $1.00P_T$, respectively) to account for an expected increased flexibility of the connection due to the flexibility of the stiffening beam and the existing boundary conditions. The Floor 3 FLC was assumed to have the same stiffness and strength as the U-shape yielding element (i.e., $1.00K_U$ and $1.00P_U$, respectively).

To account for uncertainty in the connection, variations of the force–deformation for the FLC assembly were generated from the force–deformation relationship of the yielding elements via four random variables: $X_K^1, X_P^1, X_K^3, X_P^3$. The stiffness and strength of the Floor 1 FLC were determined by $X_K^1\ K_T$ and $X_P^1\ P_T$. The stiffness and strength of the Floor 3 FLC were determined by $X_K^3 K_U$ and $X_P^3 P_U$; see Figure 5B,C. The as-built Floor 1 FLC differed from boundary conditions used to test the T-shape yielding element; thus, the stiffness factor X_K^1 was assumed to vary between 0.50 and 0.80, and the strength factor X_P^1 was assumed to vary between 0.80 and 1.20 for the Floor 1 FLC. The as-built Floor 3 FLC better matched the setup of the test for the U-shape yielding element; however, for consistency with the assumed range of variations in the Floor 1 FLC, X_K^3 and X_P^3 were assumed to vary between 0.80 and 1.20 as well.

6 | RESULTS AND DISCUSSION

The effects of modeling uncertainty were studied using the uncertainty groups from Table 3. The sensitivity of the EDPs, in terms of peak story drift ratio θ_j and peak absolute floor acceleration PFA_j at floor j, were analyzed for the deterministic model classes and continuous model parameters. The contributions of the uncertain inputs to the variance of the maximum EDP over all floor/stories EDP_{max} (i.e., $\sigma^2_{EDP_{max}}$) were summarized via the total Sobol index S_T. To visualize trends across the models and to study the particularities of the specimens, the many realizations of the spine-to-frame connection uncertainty group in the Frame–Spine and Frame–Spine–FLC specimens are then illustrated in greater detail.

TABLE 4 Modal periods computed from the numerical models and experiments.

System	Source	T1 (s)	T2 (s)	T3 (s)	T4 (s)
Frame	Numerical[a]	1.50	0.32	0.17	0.11
Frame–Spine	Numerical[a]	1.07	0.18	0.08	0.04
	[Experimental]	[1.19]	[0.20]	[0.10]	[0.06]
Frame–Spine–FLC	Numerical[a]	1.28	0.23	0.16	0.11
	[Experimental]	[1.33]	[0.23]	[0.16]	[0.12]

[a]Values correspond to the mean periods computed from the set of secondary models.

Comparisons with experimental results were used to assess the overall quality of the models. The overlapped experimental results corresponded to the filtered measurements of the two lateral force-resisting bays on opposite sides of the specimen floor plan; response histories of sensors on the same floor were averaged and zeroed out at the beginning of each test run to determine the peak response values from the experiment.[34] Although considered in other studies,[37] the numerical results presented herein did not account for residual damage or consecutive shaking of the specimens, as would be present in the experiment.

6.1 | Estimated EDP_j considering modeling uncertainty

The mean of the modal periods T_n from eigenvalue analyses of the secondary models were compared to the modal periods calculated via sensor measurements and pink noise excitation of the physical test specimens, as tabulated in Table 4. The eigenvalue analyses were conducted in the elastic range, even though the Frame–Spine–FLC physical specimen exhibited some yielding due to previous excitations during the sequential testing program.[34] Despite this inconsistency, estimates of the mean modal periods from the numerical models agreed with calculations from the experimental measurements. In the case of the Frame–Spine models, the consideration of a near-rigid spine-to-frame moment connection (i.e., C2 in Figure 4) had lower mean estimates of T_1; the more flexible connections showed a better agreement with T_1 from the experiment.

The estimated EDP_j (i.e., θ_j and PFA_j) for the Northridge and JMA Kobe records using the modeling variations were also compared to the peak experimental results. Fitted PDFs using the Generalized Extreme Value Distribution in MATLAB[79] were used to illustrate the variability of the EDP_j due to the modeling uncertainty for each specimen; see Figure 6 (specimens are indicated by color: gray for the Frame, blue for the Frame–Spine, and red for the Frame–Spine–FLC). Recall, the spectral characteristics of the two ground motion records are different; that is, the Northridge record tends to excite the higher-mode accelerations, while the JMA Kobe record tends to induce large first-mode displacements.

Overall, the numerically simulated peak response generally aligned with the experimental results. Due to the spine, the Frame–Spine models distributed θ_j more uniformly and developed smaller θ_1 than the models of the Frame, which formed a first-story mechanism, and Frame–Spine–FLC, which employed yielding elements in the FLC to reduce accelerations at the cost of minor increases in story drift. The estimated peak story drifts θ_j for the Northridge and JMA Kobe records are shown in Figure 6A,B. For the Frame specimen, θ_1 larger than 5% is not shown, because these drift levels exceeded the valid range of the numerical models and indicated the collapse vulnerability of the base MRF without spines. For both records, the Frame–Spine and Frame–Spine–FLC models avoided story mechanisms. Due to the FLC, the Frame–Spine–FLC models had less drift uniformity (i.e., θ_j increased at Story 1 and decreased at Story 4) compared to the Frame–Spine models. The estimated peak floor accelerations PFA_j for the Northridge and JMA Kobe records are shown in Figure 6C,D. For the Northridge record (Figure 6C), which produced large demands in the higher modes, the Frame–Spine–FLC models reduced PFA_j compared to the Frame–Spine models (particularly at Floor 2 and Floor 4); for the JMA Kobe record (Figure 6D), PFA_j remained closer to the PGA. PFA_j of the Frame models remained the smallest for the Northridge record, due to the first-story mechanism and the higher-mode accelerations exhibited by the other two specimens with spines (i.e., $S_a(T_2)$ for the Northridge record).

Although considered acceptable as pretest estimates, some discrepancies between the numerical and experimental results were observed. For story drifts (Figure 6A,B), the 95% confidence interval of the estimates from the Frame–Spine models represented the peak experimental data at all stories, while the Frame–Spine–FLC models represented the drifts at the first story and underestimated the drifts at the upper stories. For floor accelerations (Figure 6C,D), the 95% confidence interval of the estimates from the Frame–Spine and Frame–Spine–FLC models represented the peak results from

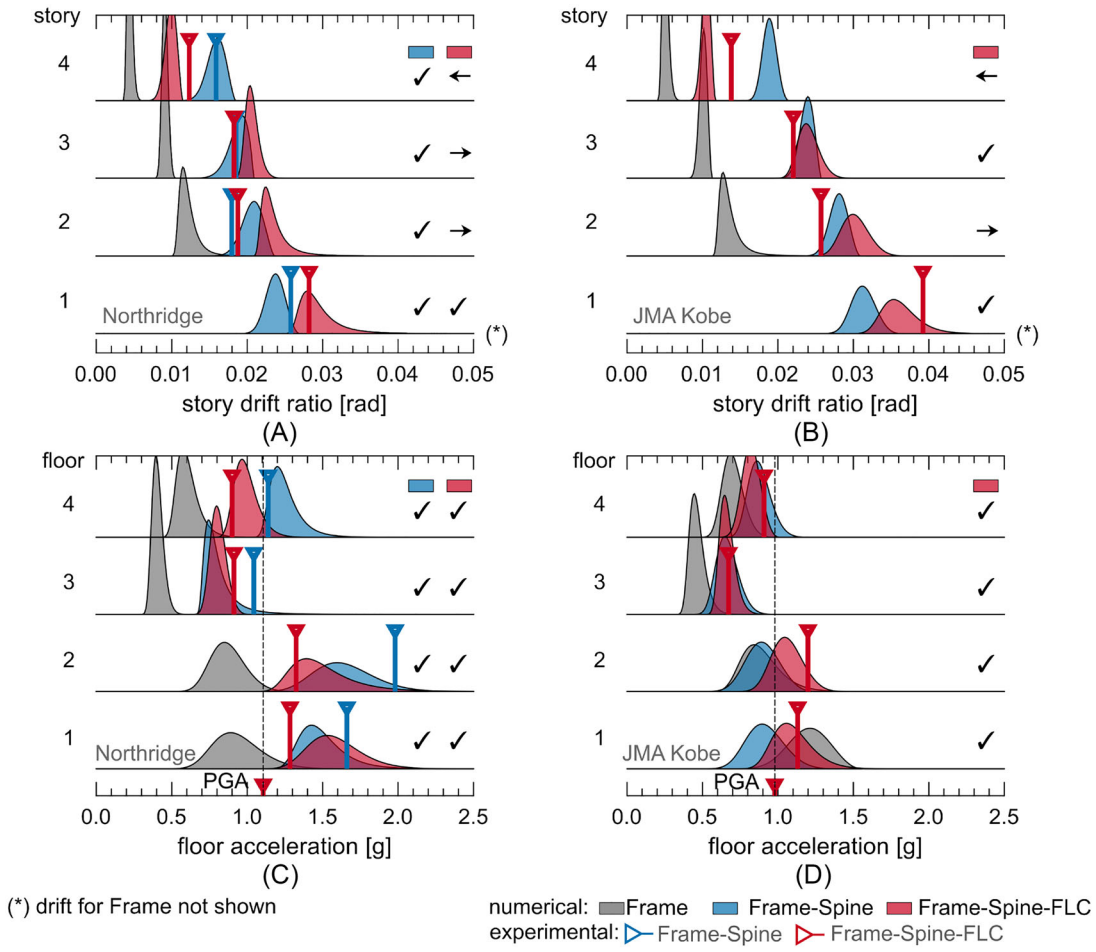

FIGURE 6 PDF of θ_j estimates considering modeling uncertainty for: (A) Northridge and (B) JMA Kobe records; PDF of PFA_j estimates considering modeling uncertainty for (C) Northridge and (D) JMA Kobe records. Side markers indicate if the experiment is within the 95% confidence interval of the numerical estimates.

TABLE 5 Mean root square error for drifts and accelerations (e_θ and e_{PFA}) comparing results from numerical models and the experiment.

System	Record	mean e_θ [rad]	min e_θ [rad]	mean e_{PFA} [g]	min e_{PFA} [g]
Frame–Spine	Northridge	0.0021	0.0016	0.26	0.10
Frame–Spine–FLC	Northridge	0.0032	0.0018	0.21	0.04
Frame–Spine–FLC	JMA Kobe	0.0037	0.0019	0.11	0.02

the experiments, although improvements could still be made after collecting the test data and refining the models based on the response histories.

The accuracy (i.e., how close the numerical simulations were to the measured values) of the θ_j and PFA_j estimates compared to the experimental results depended on the ground motion characteristics and specimen. The root-mean-square error e_{EDP} between the estimates of the numerical models and experiments is summarized in Table 5 and allows one to condense the errors across all stories/floors into one metric per simulation. On average, the drift estimates for the Frame–Spine specimen excited by the Northridge record and the floor accelerations for the Frame–Spine–FLC excited by the JMA Kobe record had the least drift and acceleration error, respectively; the first (i.e., the least drift error) corresponded to the experiment with no previous damage in the structure, and the second (i.e., the least acceleration error) corresponded to the experiment with the record that did not produce large excitations in the higher modes. Also, Table 5 illustrates how considering modeling uncertainty can be beneficial in estimating possible outcome scenarios for a particular event, with errors as low as 0.0016 rad and 0.02 g using a set of stochastically generated—but feasibly realistic—secondary models.

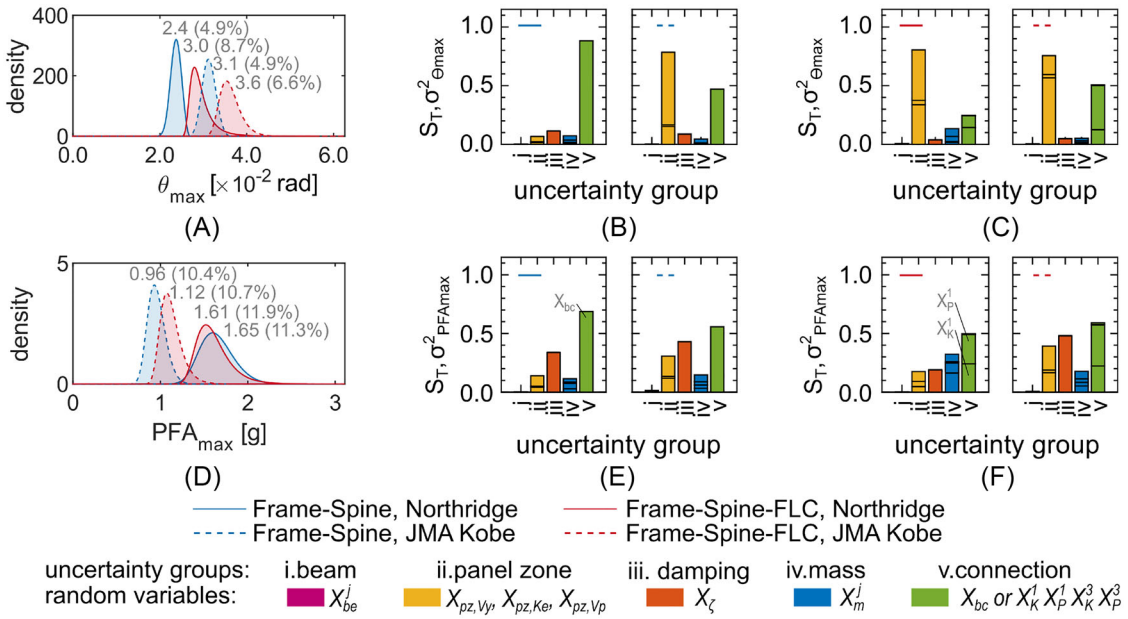

FIGURE 7 PDF of (A) θ_{max} and (D) PFA_{max}; mean and COV values are noted next to the distributions. Contribution of the Frame–Spine random variables to the uncertainty of (B) θ_{max} and (E) PFA_{max} via total Sobol indices S_T. Contribution of the Frame–Spine–FLC random variables to the uncertainty of (C) θ_{max} and (F) PFA_{max} via total Sobol indices S_T. COV, coefficient of variation; FLC, force-limiting connection.

Although this paper focuses on the propagation of modeling uncertainty, Bayesian updates of the stochastically generated models could ease modeling calibration to reproduce the experimental results by minimizing the error metrics from Table 5 (e.g., as in Muto and Beck[80]).

6.2 | Variation of EDP_{max} considering modeling uncertainty

The addition of modeling uncertainty leads to variations in the estimates of the EDP. As incorporating modeling uncertainty can lead to large amounts of data, the coefficient of variation $COV_{EDP} = \sigma_{EDP}/\mu_{EDP}$ can be used to interpret variations in the estimated EDP due to changes in the numerical model. The distribution of the peak results for the specimens with spines (i.e., for the Frame–Spine and Frame–Spine–FLC models) are summarized in Figure 7A,D; the mean and the COV are noted next to the PDFs. The COVs were around two times larger for estimates of PFA_{max} compared to θ_{max}. Thus, if considering modeling uncertainty only (not record-to-record variability), acceleration demands exhibited more variability than drift demands.

The decomposition of $\sigma^2_{EDP_{max}}$ and the contributions of each random variable to that variance (i.e., the total Sobol indices) are shown in Figure 7B,C,E,F for drifts and accelerations. In the plots, each stacked bar represents the total Sobol index S_T of the random variables associated with an uncertainty group of the Frame–Spine and Frame–Spine–FLC models for the Northridge or the JMA Kobe records.

The contributions of each random variable to the θ_{max} variance are shown in Figure 7B,C for the Frame–Spine and Frame–Spine–FLC models, respectively. Notably, varying X_{b_e} had little effect on the variance of drift. Except for the Frame–Spine models excited by the Northridge record, the panel zone random variables produced the largest variations of θ_{max}, because energy dissipation was primarily due to panel zone yielding. From the panel zone variables, the yielding strength and plastic strength (X_{V_y} and X_{V_p}) contributed more to the variance than the elastic stiffness (X_{Ke}). Changes in damping X_ζ and mass X_{m_j} had little effect on the variance of θ_{max}. The spine-to-frame connection, represented by the deterministic model classes of the bolted connection X_{bc} in the Frame–Spine models and by the continuous model parameters of the Frame–Spine–FLC models, was also a large contributor to $\sigma^2_{\theta_{max}}$. In particular, in the Frame–Spine–FLC, the Floor 1 FLC stiffness and strength (X^1_K and X^1_P) were larger contributors to the $\sigma^2_{\theta_{max}}$ than the Floor 3 FLC stiffness and strength (X^3_K and X^3_P); that is, θ_{max} was sensitive to variations of X^1_K and X^1_P.

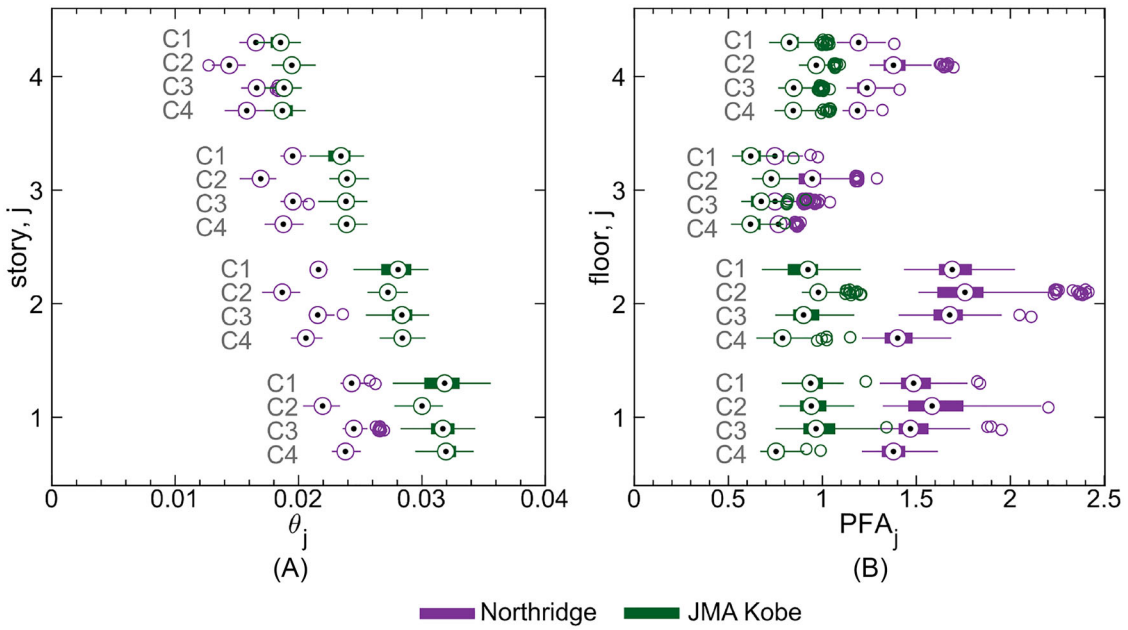

FIGURE 8 Effect of bolted connection model classes (A) story drifts (B) floor accelerations in the Frame–Spine model. The condensed box plots summarize the median, 25th and 75th percentiles, minimum, maximum, and outliers of the estimates.

The contributions of each random variable to the PFA_{max} variance are shown in Figure 7E,F for the Frame–Spine and Frame–Spine–FLC models, respectively. Similar to drifts, X_{b_e} had a negligible effect on the variance of accelerations. The panel zone strength random variables contributed to the $\sigma^2_{PFA_{max}}$ but with less proportion than for drifts; instead, the damping X_ζ random variable played a major role in the $\sigma^2_{PFA_{max}}$. Generally, the mass X_{m_j} showed a smaller contribution to $\sigma^2_{PFA_{max}}$ compared to the other random variables; however, recall the mass was only changed to within ±5% the nominal estimate. The spine-to-frame connection remained a large contributor to $\sigma^2_{PFA_{max}}$; the model classes of the bolted connection were the largest contributor to the variance of the acceleration in the Frame–Spine models, while the Floor 1 FLC stiffness and strength (X^1_K and X^1_P) were important in the variance of the acceleration in the Frame–Spine–FLC models.

6.3 | Effects of the spine-to-frame model classes in the Frame–Spine model

The effects of modeling uncertainty are illustrated in detail for the spine-to-frame (bolted) connection of the Frame–Spine model, which was one of the less well-characterized parts of the seismic force-resisting system. The story/floor response corresponding to each model class is illustrated in the box plots in Figure 8; the marker colors indicate the input record. For drifts (Figure 8A), model C2 resulted in the smallest median θ_j, C3 resulted in a similar median θ_j to C1, and C4 resulted in a smaller θ_j than C1 when excited by the Northridge record. Additionally, C3 has more outliers than the other model classes for the Northridge record, meaning that larger θ_j could occur if the Floor 1 bolted connection experiences nonlinear behavior but the bolted connections at other floors do not (i.e., C3); such outliers are not present if nonlinear behavior is also allowed at the other bolted connections (i.e., C4). For accelerations (Figure 8B), typically, model C2 resulted in the largest median PFA_j, C3 resulted in a similar median PFA_j to C1, and C4 resulted in the smallest PFA_j. The near-rigid moment connection also shows the largest outliers, particularly in PFA_2 when excited by the Northridge record, where some estimates almost reached 2.5 g. Additionally, if nonlinear response occurred in the bolted connection at all stories (i.e., C4), peak floor accelerations are expected to be less than if the bolted connection was modeled as pinned (i.e., C1).

In summary, if the bolted connection was modeled as near-rigid in flexure (i.e., C2), the peak drifts and floor accelerations would be smaller or larger, respectively, than if the bolted connection was modeled as pinned or as partially restrained. The numerical simulations suggest that the idealizations of the moment transfer between the spine and the frame could significantly impact estimates of both drifts and accelerations for systems employing spines. Note, however,

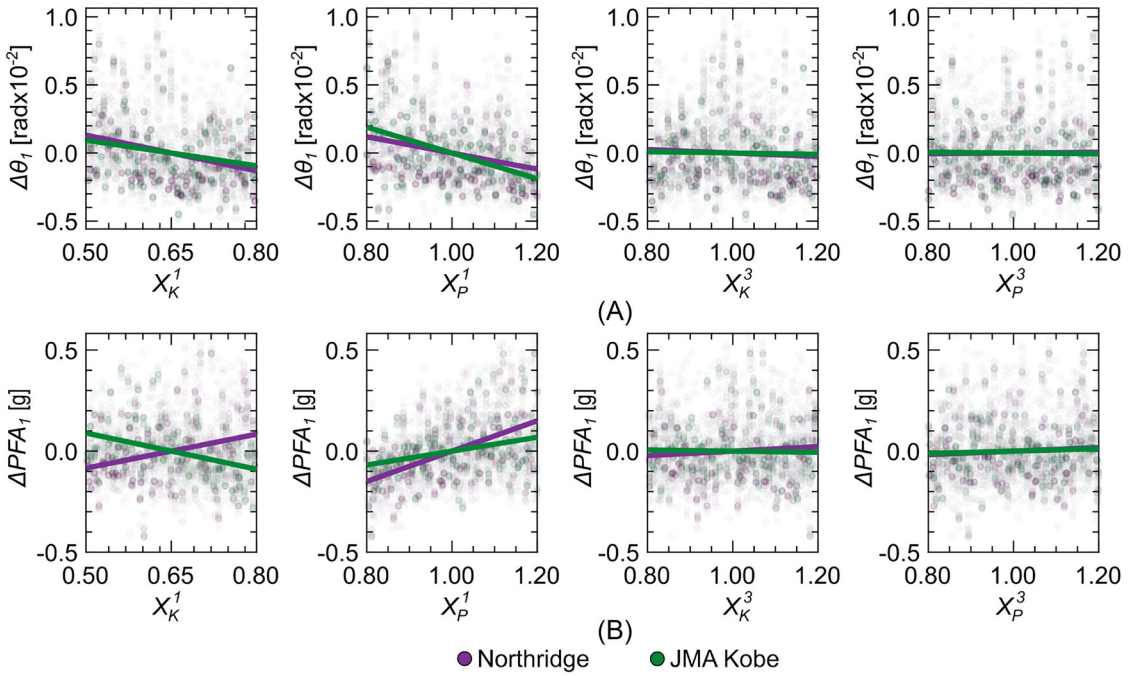

FIGURE 9 Effect of FLC model parameters on (A) the first-story drift ratio θ_1 and (B) the first-floor accelerations PFA_1 of the Frame–Spine–FLC model. The mean θ_1 and PFA_1 were subtracted from the realizations and noted as $\Delta\theta_1$ and ΔPFA_1. The overlapped lines have a slope equal to $\rho_{X_i,EDP_j}\sigma_{EDP_j}/\sigma_{X_i}$. FLC, force-limiting connection.

that the results are only applicable to the specimens under study. Further studies are needed to then explore the detailing of the spine-to-frame bolted connection for designing and modeling purposes based on this finding.

6.4 | Effects of the spine-to-frame model parameters in the Frame–Spine–FLC model

Uncertainty due to the spine-to-frame (force-limiting) connection was also characterized in more detail in the Frame–Spine–FLC models. The ρ coefficient is used to represent the relation between the FLC model parameters and the EDPs using all the samples. The sensitivity of the EDPs to the spine-to-frame model parameters was analyzed using uncorrelated input random variables, which allows the analysis to illustrate the effect of each variable separately to gain intuition on its characteristic effect on the EDPs; results still account for the interaction of random variables, but results attributed to one variable are not being driven by the changes in other variables because of their independence.

Correlation between the numerical model inputs and outputs can be observed by the spread of the data scatter in Figure 9; the *x*-axis corresponds to the spine-to-frame FLC random variables (X_K^1, X_P^1, X_K^3, X_P^3), the *y*-axis to the first story/floor EDPs (θ_1 and PFA_j), and the overlapped lines have a slope equal to $\rho_{X_i,EDP_j}\sigma_{EDP_j}/\sigma_{X_i}$. To focus on changes in the EDPs due to each variable, the mean estimate of the EDP_j was subtracted from all the realizations and denoted by ΔEDP_j (in this case, $\Delta\theta_j$ in Figure 9A and ΔPFA_j in Figure 9B). From these plots, the larger the X_K^1, the smaller the θ_1 for both records (i.e., negatively correlated), the larger the PFA_1 for the Northridge record and the smaller the PFA_1 for the JMA Kobe record (i.e., positively and negatively correlated, respectively). These results suggest that a stiffer Floor 1 FLC results in reduced first-story drift, but the relation with the first-story acceleration may be ground-motion-dependent. For strength, the larger the X_P^1, the smaller the θ_1 and the larger the PFA_1 for both records; suggesting a weaker FLC would reduce PFA_1 at the cost of increasing θ_1. In addition, θ_1 and PFA_1 exhibited smaller correlations with X_K^3 and X_P^3, indicating that the first floor/story response was less related to the model parameters of the Floor 3 FLC compared to the Floor 1 FLC.

Figure 10 expands the analysis of correlations to other stories/floors (i.e., θ_j and PFA_j). X_K^1 exhibited a negative correlation with θ_1 and positive correlation with θ_4 for both records; additionally, X_K^1 exhibited a positive correlation with PFA_j for the Northridge record, and a negative correlations with PFA_j for the JMA Kobe record. Thus, a softer Floor 1 FLC results in increased drifts at the bottom stories and reduced drifts at the upper stories (expected due to the loss of drift

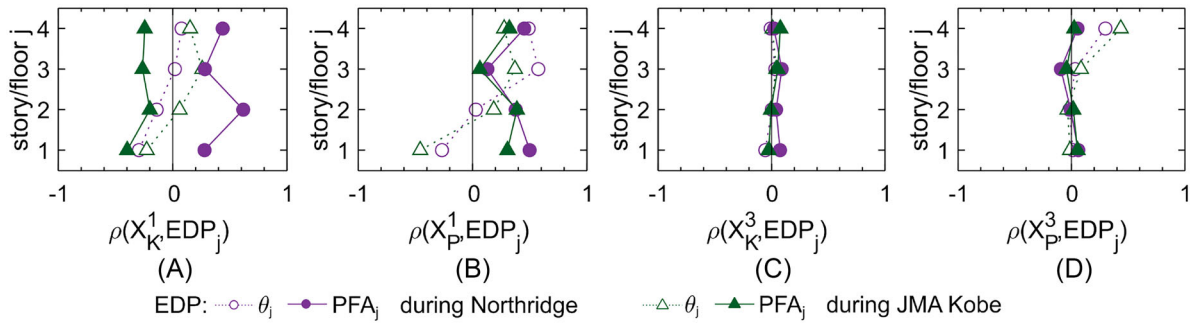

FIGURE 10 Correlation between FLC model parameters and EDP estimates. (A) Stiffness of Floor 1 FLC, X_K^1; (B) strength of Floor 1 FLC, X_P^1; (C) stiffness of Floor 3 FLC, X_K^3; (D) strength of Floor 3 FLC, X_P^3. EDP, Engineering Demand Parameter; FLC, force-limiting connection.

uniformity), along with reduced peak floor accelerations for the Northridge record (expected due to higher-mode mitigation). X_P^1 exhibited a negative correlation with θ_1 and a positive correlation with θ_4 for both records. Additionally, X_P^1 exhibited a positive correlation with PFA_j for both records, particularly at the lower floor and roof levels. Thus, a weaker Floor 1 FLC results in a loss of drift uniformity but also reduced $PFA_{1,2,4}$ compared to the mean EDP estimates (which are again associated with higher-mode accelerations). Regarding the Floor 3 FLC, X_K^3 did not exhibit a strong correlation with any EDP, while X_P^3 exhibited a strong positive correlation with θ_4, particularly for the JMA Kobe record; thus, the Floor 3 stiffness is not of particular interest (in the domain of study) and a weaker Floor 3 FLC would reduce θ_4 with little influence on PFA.

The numerical simulations suggest that the stiffness, strength, and placement of the FLC between the spine and the frame affect both drift and acceleration estimates. Although the results are specific to these specimens, further studies can explore the optimal location and design of FLC for a larger set of design archetypes and ground motion records (including records that produce similar large higher-mode effects like the Northridge record).

7 | CONCLUSIONS

Numerical models provide insights into the dynamic response of structures. However, modeling uncertainties can lead to variability in the numerical response, particularly for less well-established structural systems or components, affecting estimates of the seismic demands needed for design and performance assessments. Herein, sources of modeling uncertainty were identified for three test specimens, namely the Frame, Frame–Spine, and Frame–Spine–FLC specimens, where the latter two were physically tested at the E-Defense shake table in Japan. The inelastic response of the MRF Frame specimen was expected to concentrate in the panel zones. Modeling variations using deterministic model classes and continuous model parameters were used to explicitly address uncertainties in modeling the beam composite action, panel zone behavior, target damping ratio, mass, and spine-to-frame connections. Dispersion of the EDP estimates (i.e., peak story drifts and peak floor accelerations) were illustrated using the coefficient of variation, variance, and Sobol Index to identify which model features most affect the numerical response. Correlations of the EDP to the model parameters were then used to gain an intuition of the effects of those model parameters. Explicitly incorporating modeling uncertainty enabled more robust estimates of the range of possible structural response in support of the shake-table testing program and can be used to identify important model features for future numerical studies.

Observations and conclusions are summarized below:

- The trends of the peak story drifts were similar for all the models; the Frame models exhibited a tendency to form a first-story mechanism, and the addition of the spines distributed drifts more uniformly, avoided excessive drift concentrations, and mitigated a story mechanism, regardless of the spine-to-frame connection detail (i.e., bolted connection or FLC). In comparing the systems with spines, the Frame–Spine models tended to have more uniform story drifts, with reduced story drifts at the lower stories and increased story drifts at the upper stories, compared to the Frame–Spine–FLC models. Upon comparison with the experimental results using the 95% Confidence Interval and root-mean-square error, the story drifts from the secondary Frame–Spine models aligned with the experimental results, while the

secondary Frame–Spine–FLC models were able to represent the first-story drift but typically underestimated the upper story drifts. Models can now be refined post-test to better represent the upper story response.

- Unlike story drift ratio, the trends of the peak floor accelerations differed depending on the ground motion record. With the Northridge record, the addition of spines resulted in increased accelerations above the PGA for the Frame–Spine and Frame–Spine–FLC models compared to the Frame model due to large spectral content near the higher-mode periods and near-elastic higher-mode effects.[46] On average, the maximum floor acceleration was smaller for the Frame–Spine–FLC models than for the Frame–Spine models; using the FLC in the Frame–Spine–FLC models aided in reducing the large floor acceleration at the second floor of the Frame–Spine models, although many models resulted in increased accelerations at the first floor depending on the parameters used to model the FLC. With the JMA Kobe record, floor accelerations tended to be smaller than for the Northridge record and closer to the PGA for all the models, because the JMA Kobe record had less spectral content near the higher-mode periods. Overall, the numerically simulated behavior using the models aligned with the experimental results for the peak floor accelerations in terms of the 95% confidence interval and root-mean-square error, with the largest errors occurring for the Northridge record.
- Metrics like the coefficient of variation (COV), variance, and Sobol Index can be used to succinctly identify model features most affecting the numerical response quantities of interest. Generally, the COV for the estimates of story drift was smaller than for floor accelerations using the secondary models. In assessing modeling uncertainty with the Sobol Index, models of the spine-to-frame connection and panel zone strength had the largest effect on the dispersion of the story drifts, while models of the spine-to-frame connection, target damping ratio, and panel zone had the largest effect on the dispersion of the floor accelerations. The dependency of the building response to the spine-to-frame bolted connection and FLC suggests that the model of the attachment between the spines and the frame may need to be carefully considered in future studies of systems employing spines and FLC.
- The Linear Pearson correlation coefficient, ρ, can be used to correlate variations in the modeling parameters to variations in the EDP estimates. For example, for the Frame–Spine–FLC models, the Floor 1 FLC had a stronger correlation with the EDP estimates at all floors than the Floor 3 FLC. Increased stiffness of the Floor 1 FLC resulted in smaller lower-story drifts and larger upper-story drifts for both records; the effect on floor accelerations was ground-motion-dependent. Increased strength in the Floor 1 FLC resulted in similar trends as increased stiffness for story drifts, but increased strength also resulted in larger floor accelerations at all floors, regardless of the record. Modeling of the Floor 3 FLC stiffness had little influence on drifts or accelerations, and increased strength of the Floor 3 FLC resulted in decreased upper story drifts with little influence on floor accelerations. Thus, the placement and design of the FLC could be optimized to meet a certain target response.

Identifying sources of modeling uncertainty and assessing their effects on EDPs is important to the assessment of new lateral force-resisting systems and their devices. The observations presented herein used a reduced number of simulations and are limited to the particular specimens built for testing purposes; however, the methods of interpreting data presented herein contribute to the performance-based design and assessment of new systems including modeling uncertainty, especially those employing spines and FLC. Results can be used to initially select those model features most important to estimates of the response of systems employing spines and FLC, potentially informing future design methodologies in conjunction with a larger set of design prototypes, increased numerical simulations, and incorporation of record-to-record variability. The approach used herein to address modeling uncertainty can also be used to enable more robust estimates of structural response, for example, to inform the design and preparation of future experiments. Further studies could propagate modeling uncertainty in a similar manner for other structural systems, using different uncertainty groups and including more refined PDFs and informed correlations for the input random variables based on a larger set of test data.

ACKNOWLEDGMENTS

The research presented in this paper is funded by the U.S. National Science Foundation under the project Collaborative Research: Frame-Spine System with Force-Limiting Connections for Low-Damage Seismic-Resilient Buildings (CMMI 1928906, 1926326, and 1926365), and additional support is provided by the American Institute of Steel Construction, Nippon Steel Engineering, the Disaster Prevention Research Institute (DPRI) at Kyoto University, and JSPS KAKENHI Grant Number 20H00269. The research is also conducted in cooperation with a major Japanese research initiative, Enhancement of Resilience for Tokyo Metropolitan Area (P.I., Akira Nishitani, Waseda University), funded by the National Research Institute for Earth Science and Disaster Resilience (NIED). The support for the E-Defense test provided by many additional organizations and people is gratefully recognized: Nippon Steel, Nippon Steel Metal Products, Schuff Steel, Kouhei Hattori (Waseda University), Yoshihiro Nitta (Ashikaga University). Some of the computing for this project was performed on the

Sherlock cluster. We would like to thank Stanford University and the Stanford Research Computing Center for providing computational resources and support that contributed to these research results. The lead author gratefully acknowledges financial support by the Fulbright Foreign Student Scholarship, which is sponsored by the U.S. Department of State and the Fulbright Commission of Ecuador. Any opinions, findings, conclusions, or recommendations expressed in this paper are those of the authors and do not necessarily reflect the views of the above-mentioned participants or funding sources.

CONFLICT OF INTEREST STATEMENT

The authors declare no conflicts of interest.

DATA AVAILABILITY STATEMENT

Some or all data, models, or code that support the findings of this study are available from the corresponding author upon reasonable request.

ORCID

Bryam Astudillo https://orcid.org/0000-0003-0361-334X
Barbara Simpson https://orcid.org/0000-0002-3661-9548
Larry A. Fahnestock https://orcid.org/0000-0003-3172-2260
Richard Sause https://orcid.org/0000-0002-6143-4385
James Ricles https://orcid.org/0000-0002-1545-5898
Masahiro Kurata https://orcid.org/0000-0003-1624-1127
Taichiro Okazaki https://orcid.org/0000-0002-7866-9332
Yi Qie https://orcid.org/0000-0001-7412-4223

REFERENCES

1. Bradley BA. A critical examination of seismic response uncertainty analysis in earthquake engineering: critical examination of seismic response uncertainty analysis. *Earthq Eng Struct Dyn*. 2013;42(11):1717-1729. doi:10.1002/eqe.2331
2. Wen Y, Ellingwood B, Veneziano D, Bracci J. *Uncertainty Modeling in Earthquake Engineering*. MAE center project FD-2 report; 2003.
3. Kelly T. A blind prediction test of nonlinear analysis procedures for reinforced concrete shear walls. *Bull N Z Soc Earthq Eng*. 2007;40(3):142-159. doi:10.5459/bnzsee.40.3.142-159
4. Terzic V, Schoettler MJ, Restrepo JI, Mahin SA. *Concrete Column Blind Prediction Contest 2010: Outcomes and Observations*. PEER report 2015/01; 2015:1-145.
5. Sousa R, Almeida JP, Correia AA, Pinho R. Shake table blind prediction tests: contributions for improved fiber-based frame modelling. *J Earthq Eng*. 2020;24(9):1435-1476. doi:10.1080/13632469.2018.1466743
6. FEMA, Venture. SJ. *Recommended Seismic Design Criteria for New Steel Moment-frame Buildings*. FEMA-350. Federal Emergency Management Agency Washington; 2000.
7. Sabelli R. *Research on Improving the Design and Analysis of Earthquake-resistant Steel-braced Frames*. EERI; 2001.
8. Cornell CA, Jalayer F, Hamburger RO, Foutch DA. Probabilistic basis for 2000 SAC federal emergency management agency steel moment frame guidelines. *J Struct Eng*. 2002;128(4):526-533.
9. AISC-341. *Seismic Provisions for Structural Steel Buildings*. American Institute for Steel Construction; 2016.
10. Lee TH, Mosalam KM. Seismic demand sensitivity of reinforced concrete shear-wall building using FOSM method. *Earthq Eng Struct Dyn*. 2005;34(14):1719-1736. doi:10.1002/eqe.506
11. Grange S, Kotronis P, Mazars J. Numerical modelling of the seismic behaviour of a 7-story building: NEES benchmark. *Mater Struct*. 2008;42(10):1433. doi:10.1617/s11527-008-9462-y
12. Lignos DG, Hikino T, Matsuoka Y, Nakashima M. Collapse assessment of steel moment frames based on e-defense full-scale shake table collapse tests. *J Struct Eng*. 2013;139(1):120-132. doi:10.1061/(ASCE)ST.1943-541X.0000608
13. Alam MS, Barbosa AR. Probabilistic seismic demand assessment accounting for finite element model class uncertainty: application to a code-designed URM infilled reinforced concrete frame building. *Earthq Eng Struct Dyn*. 2018;47(15):2901-2920. doi:10.1002/eqe.3113
14. ASCE-7. *Minimum Design Loads and Associated Criteria for Buildings and Other Structures*. American Society of Civil Engineers; 2016.
15. Porter KA, Beck JL, Shaikhutdinov RV. Sensitivity of building loss estimates to major uncertain variables. *Earthq Spectra*. 2002;18(4):719-743. doi:10.1193/1.1516201
16. Liel AB, Haselton CB, Deierlein GG, Baker JW. Incorporating modeling uncertainties in the assessment of seismic collapse risk of buildings. *Struct Saf*. 2009;31(2):197-211. doi:10.1016/j.strusafe.2008.06.002
17. Celik OC, Ellingwood BR. Seismic fragilities for non-ductile reinforced concrete frames—role of aleatoric and epistemic uncertainties. *Struct Saf*. 2010;32(1):1-12. doi:10.1016/j.strusafe.2009.04.003
18. Gokkaya BU, Baker JW, Deierlein GG. Quantifying the impacts of modeling uncertainties on the seismic drift demands and collapse risk of buildings with implications on seismic design checks. *Earthq Eng Struct Dyn*. 2016;45(10):1661-1683. doi:10.1002/eqe.2740

19. LA Ribeiro F, R Barbosa A, C Neves L. Fragility assessment of pre-northridge steel moment frames using finite-length plastic hinge elements and concentrated plasticity fracture elements. *Comput Model Eng Sci*. 2019;120(3):657-676. doi:10.32604/cmes.2019.06296
20. Dastmalchi S, Burton HV. Effect of modeling uncertainty on multi-limit state performance of controlled rocking steel braced frames. *J Building Eng*. 2021;39:102308. doi:10.1016/j.jobe.2021.102308
21. P-695 F. *Quantification of Building Seismic Performance FACTORS*. Federal Emergency Management Agency; 2009.
22. FEMA. *Seismic Performance Assessment of Buildings, Columne 1 —Methodology*. FEMA P-58-1. Applied Technology Council for the Federal Emergency Management Agency; 2018.
23. Lignos DG. Modeling and experimental validation of a full scale 5-story steel building equipped with triple friction pendulum bearings: E-defense blind analysis competition. In: *Proc., 9th Int. Conf. on Urban Earthquake Engineering (9CUEE) and 4th Asia Conf. on Earthquake Engineering*. Tokyo, Japan; 2012.
24. Dao ND, Ryan KL. Computational simulation of a full-scale, fixed-base, and isolated-base steel moment frame building tested at E-defense. *J Struct Eng*. 2014;140(8). doi:10.1061/(ASCE)ST.1943-541X.0000922
25. Flores FX, Astudillo BX, Pozo S. Effective modeling of special steel moment frames for the evaluation of seismically induced floor accelerations. *J Struct Eng*. 2021;147(1):04020311. doi:10.1061/(ASCE)ST.1943-541X.0002851
26. Chang SE, Taylor JE, Elwood KJ, Seville E, Brunsdon D, Gartner M. Urban disaster recovery in christchurch: the central business district cordon and other critical decisions. *Earthq Spectra*. 2014;30(1):513-532. doi:10.1193/022413EQS050M
27. MacRae GA, Clifton GC, Bruneau M. New Zealand research applications of, and developments in, low damage technology for steel structures. *Key Eng Mater*. 2018;763:3-10. doi:10.4028/www.scientific.net/KEM.763.3
28. Marquis F, Kim JJ, Elwood KJ, Chang SE. Understanding post-earthquake decisions on multi-storey concrete buildings in Christchurch, New Zealand. *Bull Earthq Eng*. 2017;15(2):731-758. doi:10.1007/s10518-015-9772-8
29. Earthquake Engineering Research Institute (EERI). *Functional Recovery: A Conceptual Framework with Policy Options*. Earthquake Engineering Research Institute; 2019.
30. Register F. *Executive Order 13717 of Feb 2, 2016: Establishing a Federal Earthquake Risk Management Standard. Presidential Document*. Technical report. Executive Office of the President; 2016.
31. Hayes Jr JJR, McCabe S, Mahoney M. *Implementation Guidelines for Executive Order 13717: Establishing a Federal Earthquake Risk Management Standard*. 2017. doi:10.6028/NIST.TN.1922
32. Deierlein G, Reinhorn A, Willford M. *Nonlinear Structural Analysis for Seismic Design. NEHRP Seismic Design Technical Brief No. 4*. NIST GCR 10-917-5. 2010. Produced by the NEHRP Consultants Joint Venture, a Partnership of the Applied Technology Council and the Consortium of Universities for Research in Earthquake Engineering, for the National Institute of Standards and Technology.
33. NIST. *Nonlinear Analysis Research and Development Program for Performance-Based Seismic Engineering*. Technical report. NIST GCR 14-917-27. 2017. produced by the NEHRP Consultants Joint Venture, a joint venture of the Applied Technology Council (ATC) and the Consortium of Universities for Research in Earthquake Engineering (CUREE).
34. Fahnestock L, Sause R, Ricles J, et al. U.S.-Japan collaboration for shake table testing of a Frame-Spine system with force-limiting connections. In: 17th WCEE World Conference on Earthquake Engineering, Sendai, Japan. 2021.
35. Fahnestock L, Sause R, Ricles J, et al. Frame-Spine System with Force-limiting connections for low-damage seismic-resilient buildings. In: Mazzolani FM, Dubina D, Stratan A, eds. *Proceedings of the 10th International Conference on Behaviour of Steel Structures in Seismic Areas*, Cham. 262:804-811. Springer International Publishing; 2022.
36. Rivera D. *Numerical Analysis of a Spine as a Retrofit of a Moment-Resisting Frame*. Master thesis. Oregon State University; 2020.
37. Astudillo B. *Numerical Characterization and Modeling Uncertainty of Frame-Spine and Frame-Spine-FLC Full-Scale Specimens Tested at E-Defense Shake-Table*. Master thesis. Oregon State University; 2022.
38. Lai JW, Mahin SA. Strongback system: a way to reduce damage concentration in steel-braced frames. *J Struct Eng*. 2015;141(9):04014223. doi:10.1061/(ASCE)ST.1943-541X.0001198
39. Mar D. Design examples using mode shaping spines for frame and wall buildings. In: *Proceedings of the 9th US National and 10th Canadian Conference on Earthquake Engineering*. Toronto, Canada; 2010:25-29.
40. Panian L, Bucci N, Tipping S. BRBM Frames: an improved approach to seismic-resistant design using buckling-restrained braces. In: *Structures Congress*. 2017:60-71. doi:10.1061/9780784480410.006
41. Simpson BG, Mahin SA. Experimental and numerical evaluation of older chevron concentrically braced frames with hollow and concrete-filled braces. *J Struct Eng*. 2018;144(3):04018007. doi:10.1061/(ASCE)ST.1943-541X.0001988
42. Deierlein G, Krawinkler H, Ma X, et al. Earthquake resilient steel braced frames with controlled rocking and energy dissipating fuses. *Steel Constr*. 2011;4(3):171-175. doi:10.1002/stco.201110023
43. Tsampras G, Sause R, Zhang D, et al. Development of deformable connection for earthquake-resistant buildings to reduce floor accelerations and force responses. *Earthq Eng Struct Dyn*. 2016;45(9):1473-1494. doi:10.1002/eqe.2718
44. Zhang Z, Fleischman RB, Restrepo JI, et al. Shake-table test performance of an inertial force-limiting floor anchorage system. *Earthq Eng Struct Dyn*. 2018;47(10):1987-2011. doi:10.1002/eqe.3047
45. Kawai A, Maeda T, Takewaki I. Smart seismic control system for high-rise buildings using large-stroke viscous dampers through connection to strong-back core frame. *Front Built Environ*. 2020;6:29.
46. Simpson BG. Higher-mode force response in multi-story strongback-braced frames. *Earthq Eng Struct Dyn*. 2020;49(14):1406-1427. doi:10.1002/eqe.3310

47. Fahnestock L, Sause R, Ricles J, et al. Full-scale seismic stability evaluation of a frame-spine system with force-limiting connections. In: Proceedings of the Annual Stability Conference Structural Stability Research Council, Louisville, Kentucky. 2021.
48. Sobol IM. Global sensitivity indices for nonlinear mathematical models and their Monte Carlo estimates. *Math Comput Simul*. 2001;55(1-3):271-280.
49. Ellingwood B. *Development of a Probability based Load Criterion for American National Standard A58: Building Code Requirements for Minimum Design Loads in Buildings and Other Structures*. 577. Department of Commerce, National Bureau of Standards; 1980.
50. Haselton CB, Goulet CA, Mitrani-Reiser J, et al. *An Assessment to Benchmark the Seismic Performance of a Code-conforming Reinforced-concrete Moment-frame Building*. 2007/1. Pacific Earthquake Engineering Research Center. 2008.
51. Gokkaya B, Baker J, Deierlein G. Estimation and impacts of model parameter correlation for seismic performance assessment of reinforced concrete structures. *Struct Saf*. 2017;69:68-78. doi:10.1016/j.strusafe.2017.07.005
52. Arrayago I, Rasmussen KJ, Real E. Statistical analysis of the material, geometrical and imperfection characteristics of structural stainless steels and members. *J Constr Steel Res*. 2020;175:106378. doi:10.1016/j.jcsr.2020.106378
53. McKenna F, Yi rS, Satish AB, Zsarnoczay A, Gardner M, Elhaddad W. NHERI-SimCenter/quoFEM: Version 3.2.0. 2022. This work is based on material supported by the National Science Foundation under grants CMMI 1612843 and CMMI 2131111
54. Deierlein GG, McKenna F, Zsarnóczay A, et al. A Cloud-enabled application framework for simulating regional-scale impacts of natural hazards on the built environment. *Front Built Environ*. 2020;6. doi:10.3389/fbuil.2020.558706
55. Adams B, Bohnhoff W, Dalbey K, et al. *Dakota, A Multilevel Parallel Object-Oriented Framework for Design Optimization, Parameter Estimation, Uncertainty Quantification, and Sensitivity Analysis: Version 6.13 User's Manual*. Technical report. Sandia National Lab. (SNL-NM); 2020.
56. Helton JC, Davis FJ. Latin hypercube sampling and the propagation of uncertainty in analyses of complex systems. *Reliab Eng Syst Saf*. 2003;81(1):23-69.
57. Saltelli A, Tarantola S, Campolongo F, Ratto M. *Sensitivity Analysis in Practice: A Guide to Assessing Scientific Models*. 1. Wiley Online Library; 2004.
58. Saltelli A, Annoni P, Azzini I, Campolongo F, Ratto M, Tarantola S. Variance based sensitivity analysis of model output. Design and estimator for the total sensitivity index. *Comput Phys Commun*. 2010;181(2):259-270.
59. Rivera Torres D, Simpson B. Preliminary numerical analysis of a strongback column as a retrofit of a moment-resisting frame. In: WCEE20 World Conference on Earthquake Engineering, Sendai, Japan. 2020.
60. McKenna F, Scott MH, Fenves GL. Nonlinear finite-element analysis software architecture using object composition. *J Comput Civ Eng*. 2010;24(1):95-107. doi:10.1061/(ASCE)CP.1943-5487.0000002
61. Kurata M, Kawamata Y, Kanao I, Otsuru S, Akazawa M, Gipson G. *Blind Prediction Competition 2020. Integrated Complex Structural/Non-Structural Assessment on Steel Hospital Building*. 2020.
62. Suzuki K, Watanabe A, Saeki E. *Development of U-shaped Steel Damper for Seismic Isolation System*. Technical report. Nippon Steel; 2005;92:56-61.
63. AISC-360. *Specification for Structural Steel Buildings*. American Institute for Steel Construction; 2016.
64. Brosnan DP, Uang CM. Effective width of composite L-beams in buildings. *Eng J*. 1995;32(2):73-80.
65. Krawinkler H, Mohasseb S. Effects of panel zone deformations on seismic response. *J Constr Steel Res*. 1987;8:233-250. doi:10.1016/0143-974X(87)90060-5
66. AIJ. *AIJ Recommendations for Design of Connections in Steel Structures*. Draft ed. AIJ; 2012.
67. Arakida R, Chan I, Koetaka Y. Full plastic strength of square hollow section panel zone under arbitrary directional shear force. *J Struct Constr Eng*. 2019;84(755):85-95. doi:10.3130/aijs.84.85
68. Chan I, Koetaka Y. Analytical model for joint panels with square steel tubes under bi-directional shear forces and bending moments. *J Struct Constr Eng*. 2018;83(745):503-513. doi:10.3130/aijs.83.503
69. Wang Y, Arakida R, Chan I, Koetaka Y, Nakano T. Cyclic behavior of panel zone in beam-column subassemblies subjected to bidirectional loading. *J Constr Steel Res*. 2018;143:32-45. doi:10.1016/j.jcsr.2017.12.017
70. Wang Y, Koetaka Y, Chan I, Nakano T. Elasto-plastic behavior of weak-panel beam-column joints with RC slabs under bidirectional loading. *J Constr Steel Res*. 2020;168:105880. doi:10.1016/j.jcsr.2019.105880
71. Krawinkler H, Bertero VV, Popov EP. *Inelastic Behavior of Steel Beam-to-Column Subassemblages*. 71. University of California; 1971. Issue: 7.
72. Gupta A, Krawinkler H. *Seismic Demands for the Performance Evaluation of Steel Moment Resisting Frame Structures*. Stanford University; 1998.
73. Bruneau M, Uang CM, Sabelli R. *Ductile Design of Steel Structures*. McGraw-Hill; 2011. OCLC: 870092933.
74. NIST. *Guidelines for Nonlinear Structural Analysis and Design of Buildings. Part IIa—Steel Moment Frames*. Technical report NIST GCR 17-917-46v2. National Institute of Standards and Technology; 2017
75. Newmark NM, Hall WJ. Earthquake spectra and design. *Engineering Monographs on Earthquake Criteria, Structural Design, and Strong Motion Records*. Earthquake Engineering Research Institute; 1982.
76. Bernal D, Döhler M, Kojidi SM, Kwan K, Liu Y. First mode damping ratios for buildings. *Earthq Spectra*. 2015;31(1):367-381. doi:10.1193/101812EQS311M
77. NIST. *Guidelines for Nonlinear Structural Analysis and Design of Buildings. Part I—General*. Technical report NIST GCR 17-917-46v1. National Institute of Standards and Technology; 2017.

78. ASCE-41. *Seismic Evaluation and Retrofit of Existing Buildings*. American Society of Civil Engineers; 2017.
79. *MATLAB* [Computer software]. Version 9.13.0 (R2022b). Natick, MA: The MathWorks Inc; 2022.
80. Muto M, Beck JL. Bayesian updating and model class selection for hysteretic structural models using stochastic simulation. *J Vib Control*. 2008;14(1):7-34. doi:10.1177/1077546307079400

How to cite this article: Astudillo B, Rivera D, Duke J, et al. Modeling uncertainty of specimens employing spines and force-limiting connections tested at E-defense shake table. *Earthquake Engng Struct Dyn*. 2023;1-22. https://doi.org/10.1002/eqe.3976